IEEE Photonics Journal
An IEEE Photonics Society Publication

Open Access

# Three-Axis Atomic Magnetometer Employing Longitudinal Field Modulation

Volume 9, Number 5, October 2017

Zhichao Ding
Jie Yuan
Guangfeng Lu
Yingying Li
Xingwu Long

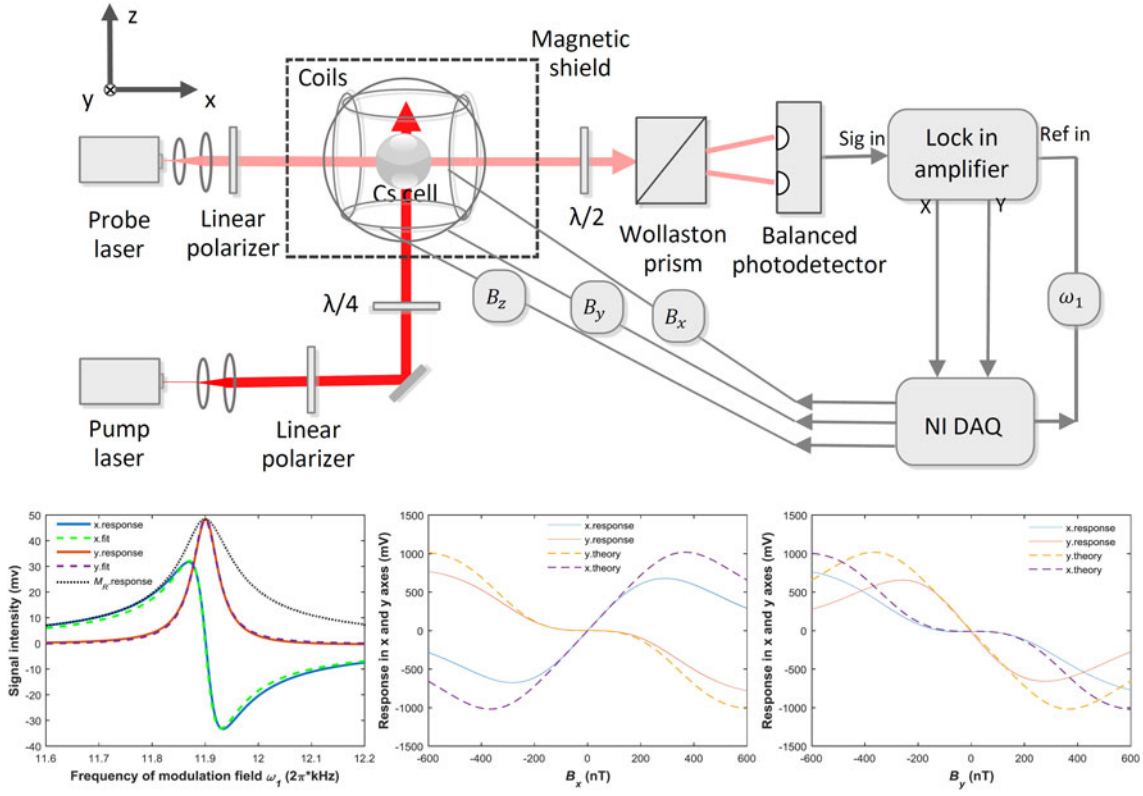


DOI: 10.1109/JPHOT.2017.2743013
1943-0655 

# Three-Axis Atomic Magnetometer Employing Longitudinal Field Modulation

**Zhichao Ding, Jie Yuan, Guangfeng Lu, Yingying Li, and Xingwu Long**

College of Optoelectronic Science and Engineering, National University of Defense Technology, Changsha 410073, China

*DOI:10.1109/JPHOT.2017.2743013*


Manuscript received June 30, 2017; revised August 16, 2017; accepted August 18, 2017. Date of publication August 22, 2017; date of current version September 12, 2017. This work was supported by the Natural National Science Foundation of China under Grant 61475192. Corresponding authors: Jie Yuan and Xingwu Long (e-mail: jieyuan@nudt.edu.cn; xwlong110@sina.com).

**Abstract:** A three-axis atomic magnetometer employing longitudinal field modulation is demonstrated theoretically and experimentally. The operational condition of this magnetometer is that the longitudinal z-component of the external magnetic field is dominant, which is achieved by applying a bias magnetic field. The longitudinal z-component of the external magnetic field is extracted from the modulation frequency, which tracks the resonance frequency, and the transverse *x*- and *y*- components are, respectively, obtained from the quadrature and the in-phase signals of a lock-in amplifier. Through feedback control, the magnitude and direction of an external magnetic field can be measured in real time, and an excellent orthogonality of the three-axis magnetometer response is obtained. By optimizing the parameters of this three-axis magnetometer, a longitudinal field sensitivity of 0.3 $pT/Hz^{1/2}$ and a transverse field sensitivity of 2 $pT/Hz^{1/2}$ are achieved.

**Index Terms:** Atomic magnetometer, magnetic resonance, modulation.

## 1. Introduction

In many significant fields, such as biomagnetism [1], geophysical exploration [2], and fundamental physics [3], it is desirable to realize the detection of weak magnetic fields. Compared with a superconducting quantum interference device (SQUID) [4], [5], an alkali-metal atomic magnetometer can achieve comparable and even higher sensitivity with non-cryogenic operation, so it is widely regarded as a more ideal option [6], [7]. SQUID can be used as a vector sensor, while the atomic magnetometer obtains the strength of a magnetic field by measuring the Larmor precession frequency of atomic spins, determining its instincts as a scalar detector. However, in many situations, knowing the strength and direction of a magnetic field is significant [8].

Different methods have been proposed to extract vector field information from a scalar atomic magnetometer [8]–[17]. Fairweather and Usher described a vector atomic magnetometer which determined the direction of a magnetic field by detecting the relative phases of the Larmor frequency modulations on two perpendicular light beams [9]. Alexandrov *et al.* realized a vector atomic magnetometer by applying a small compensating magnetic field [10]. Lenci *et al.* designed a vector atomic magnetometer based on the analysis of the coherent oscillatory transients in the transmission of resonant laser light [11].

A more common approach to extract vector field information is using parametric modulation, which can realize relatively high sensitivity due to the suppression of noise [8], [12]–[17]. By amplitude

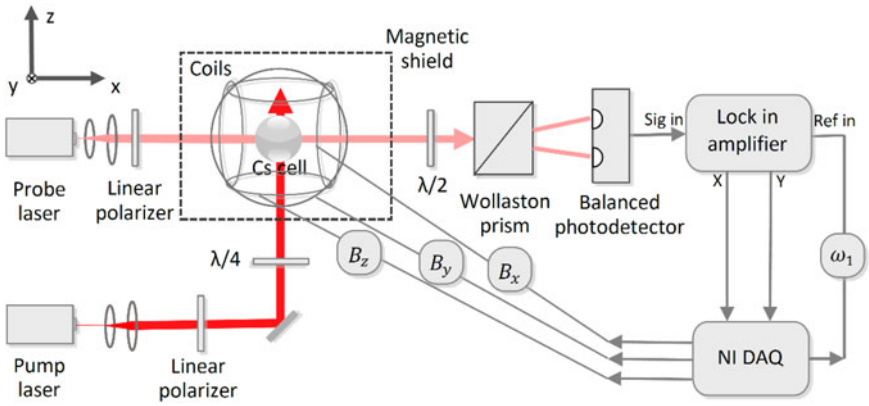


Fig. 1. Schematic diagram of the experimental setup.

modulation of two light-shift beams, Patton *et al.* demonstrated an all-optical vector magnetometer, which obtained a sensitivity of 62 $\mathrm{fT/Hz^{1/2}}$ [8]. Huang *et al.* realized a three-axis atomic magnetometer using the Bell-Bloom method, which showed an excellent orthogonality of the three-axis magnetometer response [12]. By applying two orthogonal time-varying magnetic fields modulated at different frequencies, Seltzer *et al.* designed an unshielded three-axis atomic magnetometer exhibiting a sensitivity on the order of 1 $\mathrm{pT/Hz^{1/2}}$ [14]. Pradhan described a single-beam vector atomic magnetometer by applying three orthogonal time-varying magnetic fields modulated at different frequencies [15]. Utilizing longitudinal field modulation, Li *et al.* demonstrated a two-axis atomic magnetometer which could simultaneously detect transverse *x*- and *y*- components of a magnetic field [16], and a similar kind of two-axis atomic magnetometer is used in the nuclear magnetic resonance gyroscope [17].

In this paper, we demonstrate a three-axis atomic magnetometer based on longitudinal field modulation. A theoretical model is obtained and further modified, which is helpful to analyze atomic magnetometers employing longitudinal field modulation. For realizing three-axis measurement, apart from applying a longitudinal oscillating field like [16] and [17], magnetic fields along three axes are maintained to particular values using a feedback system. Through proper operation, the longitudinal *z*-component of an external magnetic field can be extracted from the modulation frequency which tracks the resonance frequency, and the transverse *x*- and *y*- components can be respectively obtained from the quadrature and the in-phase signals of a lock-in amplifier. By optimizing the parameters of this magnetometer, it achieves a sensitivity of 0.3 $\mathrm{pT/Hz^{1/2}}$ and shows an excellent orthogonality of the three-axis magnetometer response. As our scheme only uses a single probe laser and a single modulation field, it is suitable for realizing a compact high-sensitivity three-axis atomic magnetometer.

## 2. Experimental Setup

The experimental setup is shown in Fig. 1. A spherical Pyrex cell with a diameter of 20 mm is placed inside a five-layer $\mu$-metal magnetic shield with an inner diameter of 330 cm. The cell contains $^{133}$Cs atoms and buffer gas (50 Torr $N_2$ and 50 Torr $^4$He). It is heated with a high-frequency oscillating current, and its temperature is stabilized at 60 °C. Three pairs of Helmholtz coils with diameters of 148 cm in the x-axis, 118 cm in the y-axis and 178 cm in the z-axis, driven by NI data acquisition systems (DAQ), are used to adjust the magnetic field experienced by $^{133}$Cs atoms. In addition, a modulation field $B_1 \cos(\omega_1)\hat{z}$ driven by NI DAQ is generated by the pair of Helmholtz coils along the z-axis. The Helmholtz coils can achieve a magnetic field homogeneity slightly better than $10^{-3}$ over the region of the cell. A pump beam and a probe beam are generated by two distributed feedback diode lasers which are turned to the $^{133}$Cs D1 transition, their powers are respectively 10 mW and 100 $\mu$W, and their beam sizes are respectively 0.79 $\mathrm{cm^2}$ and 0.28 $\mathrm{cm^2}$. The pump light

becomes left-circularly polarized light after passing through a linear polarizer and a $\lambda/4$ plate. Then, it polarizes the $^{133}$Cs atoms along the z-axis. After passing through a linear polarizer, the probe beam illuminates the cell. The polarization plane of the probe light is modulated due to the spin polarization of $^{133}$Cs atoms and detected using a setup involving a $\lambda/2$ plate, a Wollaston prism, and a balanced photodetector. The $\lambda/2$ plate is adjusted to zero the output of the photodetector when the pump beam and magnetic field are not applied. The detected signal is demodulated by a lock-in amplifier with the reference frequency of $\omega_1$, which is provided by the NI DAQ. The demodulated in-phase and quadrature signals are acquired by the NI DAQ.

## 3. Operational Principle

The operational condition of this three-axis atomic magnetometer is that $|B_x| \ll |B_z|$ and $|B_y| \ll |B_z|$. Under this condition, the total detected quasi-static magnetic field $B_{tot}$ is given by

$$B_{tot} = \sqrt{{B_x}^2 + {B_y}^2 + {B_z}^2} \approx B_z + \frac{B_x}{2B_z}B_x + \frac{B_y}{2B_z}B_y \approx B_z, \tag{1}$$

which is approximately along the z-axis. For achieving this condition, a bias magnetic field along the z-axis is applied. Meanwhile, a high-frequency modulation field $B_1 \cos(\omega_1 t)$ is applied along the z-axis for realizing longitudinal field modulation.

From a macroscopic view, the atomic spins can be described by a magnetization vector $\vec{M}$, which is represented as $(M_x, M_y, M_z)$ in the frame xyz. Under the influence of the external magnetic field $\vec{B}$ and pump light, the evolution of the magnetization vector is given by the Bloch equation [18]

$$\frac{d\vec{M}}{dt} = \vec{M} \times \gamma\vec{B} - \frac{M_x\hat{x} + M_y\hat{y}}{T_2} + \frac{M_0 - M_z}{T_1}\hat{z}. \tag{2}$$

Here, $\hat{x}$, $\hat{y}$ and $\hat{z}$ respectively represent the unit vectors along the x, y and z axes, $\gamma$ is the gyromagnetic ratio of atomic spins, $T_2$ and $T_1$ are respectively the transverse and longitudinal relaxation times of atomic spins, and $M_0$ is the equilibrium magnetization created by optical pumping when the modulation field is not applied. By setting $M_+ = M_x + iM_y$, it is easy to obtain

$$\frac{dM_+}{dt} = iM_z\gamma(B_x + iB_y) - \frac{M_+}{T_2} - i\gamma[B_z + B_1\cos(\omega_1 t)]M_+. \tag{3}$$

When $|B_x| \ll |B_z|$ and $|B_y| \ll |B_z|$, $M_z$ is primarily determined by optical pumping, which can be regarded as a slowly varying parameter compared with the modulation field. Under this condition, the approach of [18] can be used to solve (3), and the modulation part $\delta M_x$ of $M_x$ can be derived as

$$\delta M_x = \sum_{n=-\infty}^{\infty} \frac{T_2 M_z \gamma J_n(k_B)}{1 + (R_c T_2)^2} \sum_{p=1}^{\infty} \left\{ \begin{array}{l} [B_x R_c T_2 - B_y][J_{n+p}(k_B) + J_{n-p}(k_B)]\cos(p\omega_1 t) \\ +[B_y R_c T_2 + B_x][J_{n+p}(k_B) - J_{n-p}(k_B)]\sin(p\omega_1 t) \end{array} \right\}. \tag{4}$$

Here, $n$ and $p$ are integers, $R_c = \gamma B_z + n\omega_1$, and $k_B = \gamma B_1/\omega_1$. $J_n$, $J_{n+p}$ and $J_{n-p}$ are $n$, $n+p$ and $n-p$ orders of Bessel function, respectively. When the resonance condition $R_c = 0$ is satisfied for a proper $n$ and $\omega_1$, by ignoring other terms of $n$, (4) can be rewritten as

$$\delta M_x = T_2 M_z \gamma J_n(k_B) \sum_{p=1}^{\infty} \left\{ \begin{array}{l} -B_y[J_{n+p}(k_B) + J_{n-p}(k_B)]\cos(p\omega_1 t) \\ +B_x[J_{n+p}(k_B) - J_{n-p}(k_B)]\sin(p\omega_1 t) \end{array} \right\}. \tag{5}$$

As the detected signal of the balanced photodetector is proportional to $\delta M_x$, we can obtain $B_x$ and $B_y$ from the quadrature and the in-phase signals of a particular $p$ harmonic, respectively.

According to (4), if $B_x$ and $B_y$ are not both zero, we can obtain a dispersion signal and an absorption signal extracted from a particular $p$ harmonic, which are as a function of $\omega_1$ with the central frequency of $\omega_0 = -\gamma B_z/n$. Though we cannot track the central frequency based on phase-sensitive detection since the phase of the $p$ harmonic varies with $B_x$ and $B_y$, the root of a sum of squared dispersion and absorption signals ($M_R$ signal with the central frequency of $\omega_0$)

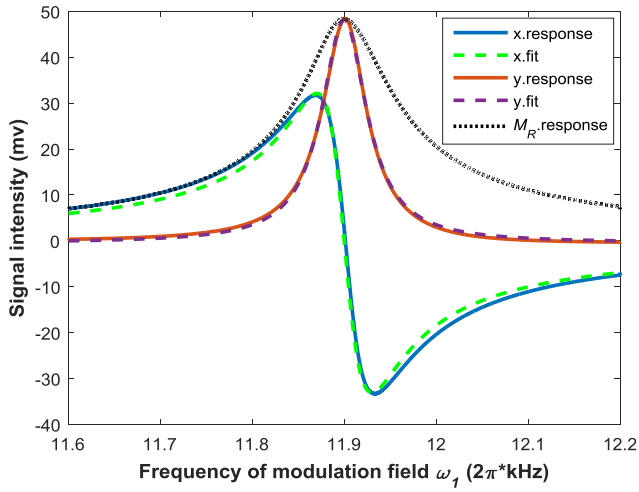


Fig. 2. Dispersion, absorption and $M_R$ signals as a function of modulation frequency $\omega_1$.

is independent of the phase. When this magnetometer operates, $n = 2$, $p = 2$ and $B_1 = 0.563\ B_z$ are selected. Substituting these conditions into (4), we can obtain $M_R \propto 1/\sqrt{1 + (R_c T_2)^2}$ since $J_{n+p}(k_B) + J_{n-p}(k_B) \approx J_{n+p}(k_B) - J_{n-p}(k_B)$, and $M_R$ is maximum when $R_c = 0$. Therefore, we can obtain $B_z$ using the scheme of $M_R$ magnetometer [19]. By adjusting $\omega_1$ until the amplitude of $M_R$ signal is maximum, we can obtain the central frequency $\omega_0$ and then deduce $B_z = -n\omega_0/\gamma$. Fig. 2 shows an example for $n = 2$ and $p = 2$ when $B_x = 0$, $B_y = -16$ nT, $B_z = 6800$ nT and $B_1 = 0.563 B_z$. The two solid lines are experimental results and the dotted line is the corresponding $M_R$ signal. The two dashed lines are fitting results using Lorentz function. As $k_B$ changes slightly when $\omega_1$ is scanned, there is a small difference between the experimental and fitting results.

Synthesizing the above conclusions, the basic operations of this three-axis magnetometer are as follows. Firstly, the central frequency of $M_R$ signal is tracked and $B_z$ is compensated to maintain it equal to 6800 nT. Then, $B_x$ and $B_y$ can be extracted from the quadrature and the in-phase signals of a particular harmonic, respectively. By feedback control, $B_x$ and $B_y$ are maintained to be equal to 0 and $-16$ nT, respectively. Repeating the above operations, $B_x$, $B_y$ and $B_z$ are obtained in real time.

For choosing optimal resonance $n$, harmonic $p$ and $B_1$, the dispersion and absorption signals under different $n$, $p$ and $B_1$ are measured when this magnetometer operates at the steady-state operating point ($B_x = 0$, $B_y = -16$ nT and $B_z = 6800$ nT). Fig. 2 shows one of the experimentally obtained results. According to (4), by fitting the absorption signals using Lorentz function and extracting their linewidths $\Delta\omega$, we can obtain corresponding $T_2$, and the results are shown in Fig. 3. In the legend of Fig. 3, n1, n2, p1 and p2 represent $n = 1$, $n = 2$, $p = 1$ and $p = 2$, respectively. As shown in (3), the modulation field influences the evolution of atomic spins and the distribution of $^{133}$Cs atoms in the ground state, thereby affecting the rate of spin-exchange collisions and causing that $T_2$ decreases with the increasing amplitude of the modulation field [20]. When the resonance condition is satisfied at $n = 1$, the modulation frequency $\omega_1 = -\gamma B_z$ is just the magnetic resonance frequency [21], which will excite atomic transitions and change the distribution of $^{133}$Cs atoms in the ground state, further increasing relaxation due to spin-exchange collisions. In addition, when the modulation frequency is the magnetic resonance frequency, as the small transverse component of the modulation field due to field inhomogeneity will induce the broadening of the absorption signal of $p = 1$ harmonic [21], $T_2$ extracted from the absorption signal of $p = 1$ harmonic is slightly smaller than the actual value. However, when the resonance condition is satisfied at other $n$ ($n > 1$), $\omega_1 = -\gamma B_z/n$ is beyond the linewidth of magnetic resonance, which will scarcely excite atomic transitions. Therefore, $T_2$ under $n = 1$ is smaller than that under other $n$.

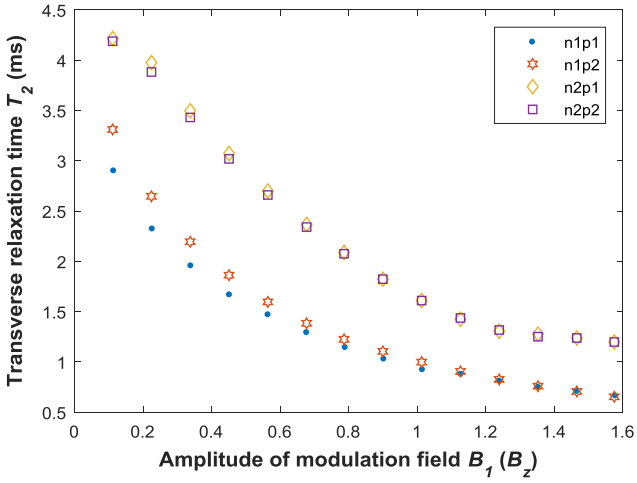


Fig. 3. Experimentally measured $T_2$ under different n, p and $B_1$.

For the measurement of the resonance frequency, the sensitivity of atomic magnetometers is proportional to $\Delta\omega/S_{NR}$, where $S_{NR}$ is the signal-to-noise ratio of the magnetic response signal. Since $\Delta\omega$ decreases with the increasing $T_2$, the sensitivity is negatively related to $T_2$ for fixed $S_{NR}$. In addition, under different $p$ and $B_1$, the maximum slope of the experimentally detected dispersion signals for $n = 2$ is 1.67 times that for $n = 1$. Therefore, in order to realize a relatively high sensitivity for the measurement of the resonance frequency, $n = 1$ is not considered. As the absolute values of $J_n(k_B)[J_{n+p}(k_B) + J_{n-p}(k_B)]$ and $J_n(k_B)[J_{n+p}(k_B) - J_{n-p}(k_B)]$ for $n > 2$ are much smaller than that for $n = 2$ when $|k_B| < 1.2$, and with the increasing of $B_1$, $T_2$ and $M_z$ decrease, in addition, it is difficulty to provide a stable high-amplitude modulation current for electronic devices, $n = 2$ is selected for our magnetometer.

As the absolute values of $J_n(k_B)[J_{n+p}(k_B) + J_{n-p}(k_B)]$ and $J_n(k_B)[J_{n+p}(k_B) - J_{n-p}(k_B)]$ for $p = 2$ are much larger than that for other $p$ when $n = 2$ and $|k_B| < 1.2$, $p = 2$ is selected. In addition, though decreasing $B_1$ can improve $T_2$, the absolute values of $J_n(k_B)[J_{n+p}(k_B) + J_{n-p}(k_B)]$ and $J_n(k_B)[J_{n+p}(k_B) - J_{n-p}(k_B)]$ for $p = 2$ will decline. So a compromise value for $B_1$ is expected. By comparing the slopes of the experimentally detected dispersion signals under different $B_1$, we find that the ratio is maximum when $B_1 = 0.563B_z$ for this magnetometer. So $B_1 = 0.563B_z$ is selected.

## 4. Performances and Analysis

For assessing the performance of this magnetometer, $B_x$ is scanned slowly when $B_y = 0$, and then $B_y$ is scanned slowly when $B_x = 0$. The responses in the x-axis (quadrature signal) and y-axis (in-phase signal) are shown with the blue solid line (x.response) and the red solid line (y.response) in Fig. 4, respectively. Unlike the magnetometer described in [16], since this magnetometer operates when the resonance condition $R_c = 0$ is satisfied, according to (4), it can realize a relatively high orthogonality of transverse field response theoretically, which is verified by the experiment. The in-phase signal almost does not respond to $B_x$ when $B_x < 100$ nT, and the quadrature signal almost does not respond to $B_y$ when $B_y < 100$ nT, showing an excellent orthogonality of transverse field response. At the steady-state operating point, this magnetometer obtains 0.14% leakage into $B_y$ when applying $B_x$ and 1.25% leakage into $B_x$ when applying $B_y$, outweighing the magnetometer described in [16] employing similar longitudinal field modulation (9.3% and 8.5%, respectively).

When $B_x$ and $B_y$ are larger than 100 nT, the response of the in-phase (quadrature) signal on $B_x$ ($B_y$) becomes large and cannot be ignored gradually, indicating that the form of (4) should be modified. Under this situation, as the magnetic resonance frequency is actually $\gamma B_{tot}$, $R_c$ should be

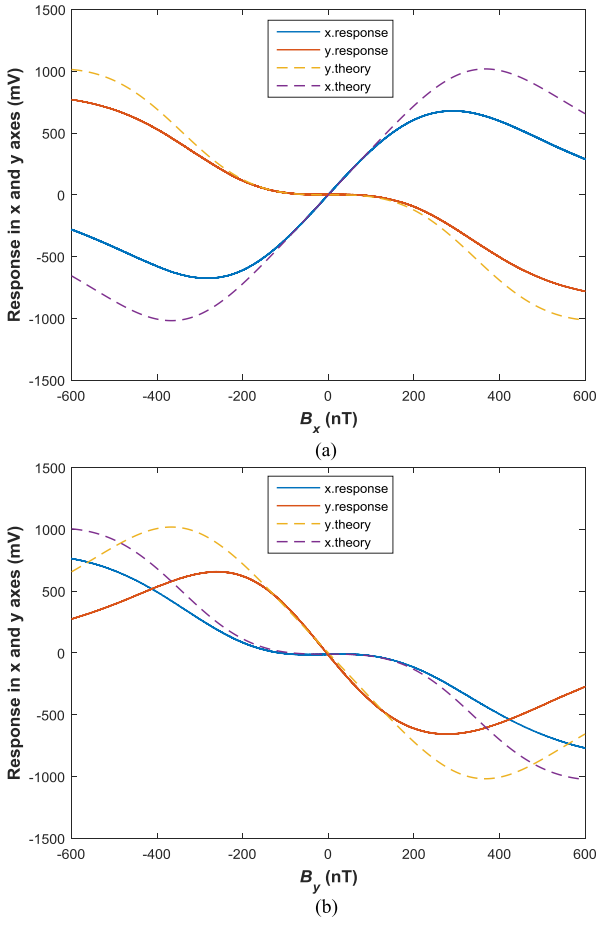


Fig. 4. Response in the x and y axes to (a) $B_x$ and (b) $B_y$.

modified as

$$R_c = \gamma B_{tot} + n\omega_1 \approx \gamma\left(B_z + \frac{B_x}{2B_z}B_x + \frac{B_y}{2B_z}B_y\right) + n\omega_1. \tag{6}$$

Substituting the conditions of $n = 2$, $p = 2$, $B_1 = 0.563B_0$, the corresponding detected $T_2 =$ 2.66 ms, and (6) into (4), we can obtain the theoretical responses in the x-axis and y-axis when $B_x$ and $B_y$ scanned, and the results are shown with dashed lines in Fig. 4. When $B_x$ and $B_y$ are large enough, there are considerable differences between theoretical and experimental results, since $B_x$ and $B_y$ will influence the values of $T_2$ and $M_z$. However, the trends of theoretical and experimental curves are similar, showing the feasibility of our modification. Therefore, the central frequency of $M_R$ signal is actually equal to $-\gamma B_{tot}/n$, and the deduced magnetic field from the central frequency is actually $B_{tot}$ rather than $B_z$. At the steady-state operating point ($B_x = 0$, $B_y = -16$ nT and $B_z = 6800$ nT), according to (1), the difference between $B_z$ and $B_{tot}$ is approximately equal to ${B_y}^2/(2B_z) \approx 19$ pT. We can correct it for obtaining more precise result.

Assuming that the transverse magnetic field jumps by 100 nT suddenly, we obtain an imprecise value of $B_z$ with the error of 735 pT when we track the central frequency for the first time. However, the transverse magnetic field will be compensated to the steady-state operating point and the readout of $B_z$ becomes accurate quickly by feedback control. In addition, as $R_c$ is maintained to be equal to zero by feedback control, leakage into the transverse magnetic field is tiny when applying $B_z$. Therefore, the cross-talk between the responses to the transverse and longitudinal magnetic fields can be ignored.

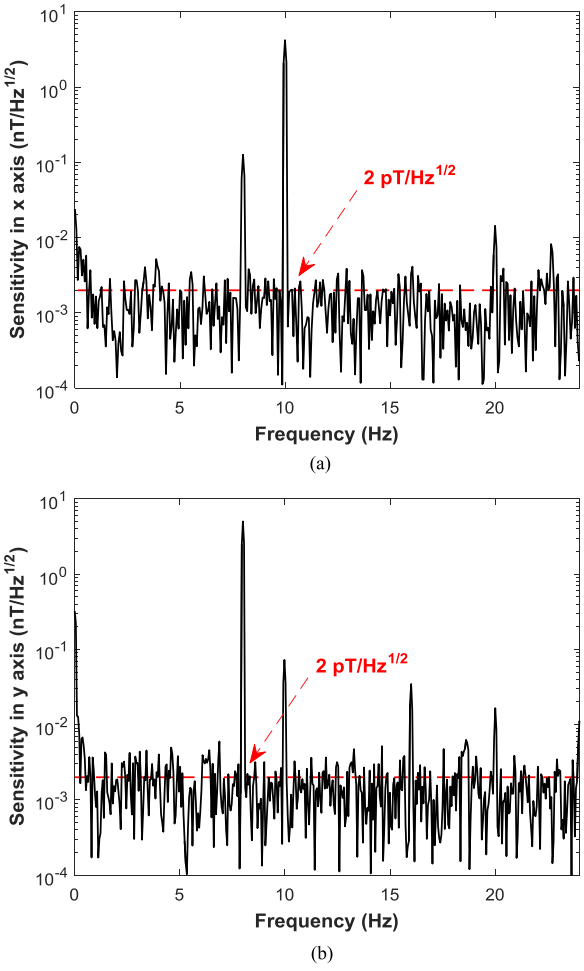


Fig. 5. Sensitivities of the three-axis magnetometer in the (a) x-axis and (b) y-axis.

The sensitivity and frequency response of this magnetometer are measured in the open-loop mode when the magnetic field experienced by the $^{133}$Cs atoms is adjusted to the steady-state operating point. Firstly, an oscillating magnetic field of 10 Hz along the x-axis and an oscillating magnetic field of 8 Hz along the y-axis are simultaneously superimposed upon the steady-state operating point, and the root-mean-square amplitudes of the two oscillating fields are 4.2 nT and 5.0 nT, respectively. By acquiring the quadrature and the in-phase signals for 100 seconds and then calculating the square roots of their power spectral densities, the magnetic response spectrums are obtained and shown in Fig. 5(a) and (b), respectively. According to the noise pedestals of the response spectrums, we can obtain that the sensitivities of the three-axis magnetometer in the x-axis and y-axis are both $2\,\mathrm{pT}/\mathrm{Hz}^{1/2}$. In addition, we obtain 1.7% leakage into $B_y$ when applying $B_x$ and 2.5% leakage into $B_x$ when applying $B_y$ in the open-loop mode. According to (4), the quadrature and the in-phase signals are respectively proportional to $B_y R_c T_2 + B_x$ and $B_x R_c T_2 - B_y$. In the open-loop mode, $R_c$ is not equal to zero any more, causing relatively large leakage factors in the open-loop mode than that at the steady-state operating point.

Then, an oscillating magnetic field of 10 Hz along the z-axis is superimposed upon the steady-state operating point, and the root-mean-square amplitude of the oscillating field is 1.6 nT. By acquiring the $M_R$ signal for 100 seconds and calculating the square root of its power spectral density, the magnetic response spectrum is obtained and shown in Fig. 6. According to the noise pedestal of the response spectrum, we can obtain that the sensitivity of the three-axis magnetometer in the z-axis is $0.3\,\mathrm{pT}/\mathrm{Hz}^{1/2}$.

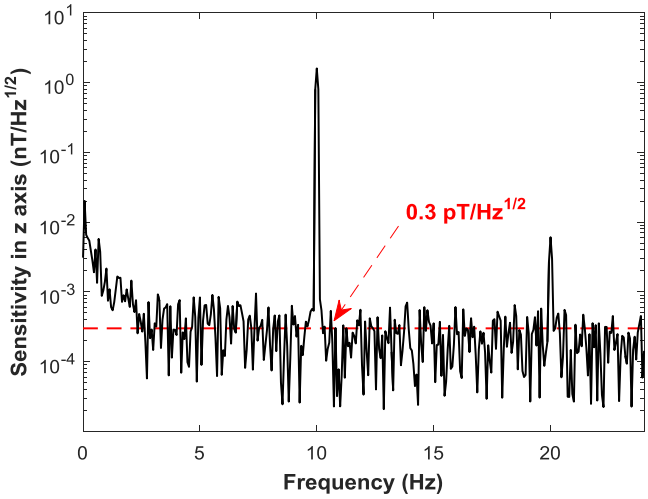


Fig. 6. Sensitivity of the three-axis magnetometer in the z-axis.

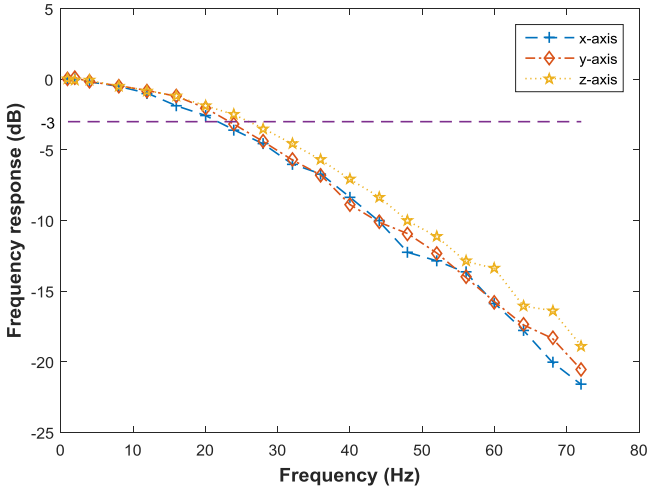


Fig. 7. Frequency response of the three-axis magnetometer.

Under ideal conditions, the polarization rotation noise $\delta\phi$ per unit bandwidth due to quantum fluctuations of the number of photons received by a balanced photodetector with 100% quantum efficiency is given by $\delta\phi = 1/\sqrt{2P_{pr}/(h\nu_{pr})}$ [22], where $\nu_{pr}$ and $P_{pr}$ are respectively the frequency and the power of probe light, and $h$ is the Planck constant. For this magnetometer, a straightforward calculation shows that $\delta\phi = 3.3 \times 10^{-8}$ rad/Hz$^{1/2}$. By calibrating the dependencies between the polarization rotations of probe light and the magnetic fields superimposed upon the steady-state operating point, the sensitivity of this magnetometer in the photon shot noise limit is estimated, which is approximately 41 fT/Hz$^{1/2}$ in the z-axis and 83 fT/Hz$^{1/2}$ in the x and y axes. The estimated result shows that the sensitivity of this magnetometer can be further improved by diminishing the technical noises, like using more stable probe and pump lasers.

By changing the frequency of the oscillating magnetic field superimposed upon the steady-state operating point and measuring the corresponding response amplitude along the x-axis, y-axis and z-axis, respectively, the frequency responses along three axes are obtained and shown in Fig. 7. The measuring bandwidths are 22 Hz in the x-axis, 23 Hz in the y-axis and 26 Hz in the z-axis. The small difference of the measuring bandwidths in the x-axis and y-axis may come from the measuring error and the different steady-state operating point of this magnetometer for $B_x$ and $B_y$.

## 5. Conclusion

In summary, we have demonstrated a three-axis atomic magnetometer employing longitudinal field modulation. The operational condition of this magnetometer is that the longitudinal z-component of the external magnetic field is dominant. For achieving this condition, a bias magnetic field along the z-axis is applied. A theoretical model is obtained and further modified, which is helpful to analyze atomic magnetometers employing longitudinal field modulation. By feedback control and optimizing the parameters of this three-axis magnetometer, it obtains 0.14% leakage into $B_y$ when applying $B_x$ and 1.25% leakage into $B_x$ when applying $B_y$, and the cross-talk between the responses to the transverse and longitudinal magnetic fields can be ignored since it is tiny, showing an excellent orthogonality of the three-axis magnetometer response. The bandwidths of this magnetometer are respectively 22 Hz in the x-axis, 23 Hz in the y-axis and 26 Hz in the z-axis. A longitudinal field sensitivity of $0.3\,\mathrm{pT/Hz^{1/2}}$ and a transverse field sensitivity of $2\,\mathrm{pT/Hz^{1/2}}$ are achieved. As our scheme only uses a single probe laser and a single modulation field, it is suitable for realizing a compact high-sensitivity three-axis atomic magnetometer.

## References


[1] C. Johnson, P. D. D. Schwindt, and M. Weisend, "Magnetoencephalography with a two-color pump-probe, fiber-coupled atomic magnetometer," *Appl. Phys. Lett.*, vol. 97, no. 24, Dec. 2010, Art. no. 243703.

[2] V. Mathé, F. Lévêque, P. E. Mathé, C. Chevallier, and Y. Pons, "Soil anomaly mapping using a cesium magnetometer: Limits in the low magnetic amplitude case," *Appl. Geophys.*, vol. 58, no. 3, pp. 202–217, Mar. 2006.

[3] J. M. Brown, S. J. Smullin, T. W. Kornack, and M. V. Romalis, "New limit on Lorentz- and CPT-violating neutron spin interactions," *Phys. Rev. Lett.*, vol. 105, no. 15, Oct. 2010, Art. no. 151604.

[4] P. John and J. Wikswo, "SQUID magnetometers for biomagnetism and nondestructive testing: Important questions and initial answers," *IEEE Trans. Appl. Supercond.*, vol. 5, no. 2, pp. 74–120, Jun. 1995.

[5] D. Robbes, "Highly sensitive magnetometers—A review," *Sens. Actuators A, Phys.*, vol. 129, pp. 86–93, Jan. 2006.

[6] I. K. Kominis, T. W. Kornack, J. C. Allred, and M. V. Romails, "A subfemtotesla multichannel atomic magnetometer," *Nature*, vol. 422, no. 6932, pp. 596–599, Apr. 2003.

[7] D. Budker and M. Romalis, "Optical magnetometry," *Nat. Phys.*, vol. 3, no. 4, pp. 227–234, Feb. 2007.

[8] B. Patton, E. Zhivun, D. C. Hovde, and D. Budker, "All-optical vector atomic magnetometer," *Phys. Rev. Lett.*, vol. 113, no. 1, Apr. 2014, Art. no. 013001.

[9] A. J. Fairweather and M. J. Usher, "A vector rubidium magnetometer," *J. Phys. E, Sci. Instrum.*, vol. 5, no. 10, pp. 986–990, May 1972.

[10] E. B. Alexandrov *et al.*, "Three-component variometer based on a scalar potassium sensor," *Meas. Sci. Technol.*, vol. 15, no. 5, pp. 918–922, Apr. 2004.

[11] L. Lenci, A. Auyuanet, S. Barreiro, P. Valente, A. Lezama, and H. Failache, "Vectorial atomic magnetometer based on coherent transients of laser absorption in Rb vapor," *Phys. Rev. A*, vol. 89, no. 4, Apr. 2014, Art. no. 043836.

[12] H. C. Huang, H. F. Dong, X. Y. Hu, L. Chen, and Y. Gao, "Three-axis atomic magnetometer based on spin precession modulation," *Appl. Phys. Lett.*, vol. 107, no. 18, Nov. 2015, Art. no. 062404.

[13] H. Huang, H. Dong, L. Chen, and Y. Gao, "Single-beam three-axis atomic magnetometer," *Appl. Phys. Lett.*, vol. 109, no. 6, pp. 227–234, Aug. 2016.

[14] S. J. Seltzer and M. V. Romalis, "Unshielded three-axis vector operation of a spin-exchange-relaxation-free atomic magnetometer," *Appl. Phys. Lett.*, vol. 85, no. 20, pp. 4804–4806, Sep. 2004.

[15] S. Pradhan, "Three axis vector atomic magnetometer utilizing polarimetric technique," *Rev. Sci. Instrum.*, vol. 87, no. 9, Aug. 2016, Art. no. 093105.

[16] Z. Li, R. T. Wakai, and T. G. Walker, "Parametric modulation of an atomic magnetometer," *Appl. Phys. Lett.*, vol. 89, no. 13, Sep. 2006, Art. no. 134105.

[17] E. J. Eklund, "Microgyroscope based on spin-polarized nuclei," Ph.D. dissertation, Univ. California, Irvine, CA, USA, 2008.

[18] C. Cohen-Tannoudji, J. Dupont-Roc, S. Haroche, and F. Laloë, "Diverses résonances de croisement de niveaux sur des atomes pompés optiquement en champ nul. I. Théorie," *Rev. Phys. Appl.*, vol. 5, no. 1, pp. 95–101, Feb. 1970.

[19] A. K. Vershovskii, S. P. Dmitriev, and A. S. Pazgalev, "Optically pumped quantum magnetometer with combined advantages of M X and M Z devices," *Tech. Phys.*, vol. 58, no. 10, pp. 1481–1488, Jan. 2013.

[20] I. M. Savukov and M. V. Romalis, "Effects of spin-exchange collisions in a high-density alkali-metal vapor in low magnetic fields," *Phys. Rev. A*, vol. 71, no. 2, Feb. 2005, Art. no. 023405.

[21] F. Bloch, "Nuclear induction," *Phys. Rev.*, vol. 70, no. 7/8, pp. 460–474, Oct. 1946.

[22] S. J. Smullin, I. M. Savukov, G. Vasilakis, R. K. Ghosh, and M. V. Romalis, "Low-noise high-density alkali-metal scalar magnetometer," *Phys. Rev. A*, vol. 80, no. 3, Sep. 2009, Art. no. 033420.